

The Potential of Hyperspectral Image Classification for Oil Spill Mapping

Xudong Kang, *Senior Member, IEEE*, Zihao Wang, Puhong Duan, *Member, IEEE*, and Xiaohui Wei

Abstract—Oil spill mapping is a very challenging problem in marine environmental monitoring. In this paper, the potential of hyperspectral image classification for mapping oil spills is comprehensively investigated. First, several representative hyperspectral image classification methods are reviewed in a general framework. Second, three oil spill mapping cases are designed to analyze the performance of different classification methods in detecting the spatial distribution, classifying the type, and estimating the thickness of oil spills. Finally, the experimental results are analyzed in detail, and some conclusions are given, which bring a comprehensive understanding to scholars who are interested in the fields of hyperspectral remote sensing and oil spill mapping.

Index Terms—Hyperspectral images, oil spill, image classification, machine learning, deep learning.

I. INTRODUCTION

With the rapid development of marine oil transportation and offshore oil exploration, oil spill accidents occur more frequently than ever before, which poses a serious threat to the ecology, environment, and so on [1]–[6]. For instance, in 1978, the Amoco Cadiz ran aground in a storm off Brittany, France, leaking about 250,000 tons of light crude oil [7]. During the 1991 Gulf War, Iraqi forces opened a valve that spilled 56,000 tons of oil into the Gulf of Mexico [8], [9]. In 2018, the “SANCHI” oil tanker collided with the bulk carrier in the East China Sea, and 130,000 tons of condensate oil spill poured into the Yangtze River, polluting 100 square kilometers of seawater [10], [11]. In 2021, the AMGhent suffered an equipment failure while refueling in the Gulf of Gibraltar, spilling 2,000 to 5,000 liters of fuel. These accidents caused by natural disasters, human activities, and equipment failures have seriously harmed ecological health and fishery development [12]–[15]. Therefore, there is a growing demand

This paper is supported by the National Key R & D Program of China (No. 2021YFA0715203), the Major Program of the National Natural Science Foundation of China (No. 61890962), the National Natural Science Foundation of China (No. 61871179 and No. 62101183), the Scientific Research Project of Hunan Education Department (No. 19B105), the National Science Foundation of Hunan Province (No. 2019JJ50036 and No. 2020GK2038), the Hunan Provincial Natural Science Foundation for Distinguished Young Scholars (No. 2021JJ022), the Huxiang Young Talents Science and Technology Innovation Program (No. 2020RC3013), the Changsha Natural Science Foundation (No. kq2202171), and the Project Funded by China Postdoctoral Science Foundation (No. 2021T140194). (*Corresponding author: Puhong Duan; Xiaohui Wei*)

X. Kang is with the School of Robotics, Hunan University, 410082 Changsha, China. e-mail: (xudong_kang@163.com).

Z. Wang, P. Duan, and X. Wei are with the College of Electrical and Information Engineering, Hunan University, 410082 Changsha, China, and also with the Key Laboratory of Visual Perception and Artificial Intelligence of Hunan Province, Changsha, 410082, China. e-mail: (w651456772@hnu.edu.cn; puhong_duan@hnu.edu.cn; xh_wei@hnu.edu.cn).

for monitoring the distribution of oil film and the levels of pollution [16]–[20].

Over the past years, many imaging techniques have been applied for oil spill monitoring, including Synthetic Aperture Radar (SAR) images [21]–[25], multi-spectral images (MSIs) [26]–[29], and hyperspectral images (HSIs) [30]–[33]. SAR images and MSIs mainly are used to detect the polluted regions while failing to distinguish different types of oil films, which limits their applications. On the contrary, hyperspectral imaging is a mushroom growing technique, which can record both abundant spectral information and finer spatial information [34]–[37]. Due to this merit, HSIs have been widely used for oil film thickness estimation and oil film type identification. Up to now, many HSI classification methods have been studied to identify different materials, such as minerals, crops, and oil films, which can be roughly divided into three categories (see Fig. 1): feature extraction, classifier, and post-processing.

Feature extraction methods aim to reduce the spectral dimension of original data and obtain discriminative spectral-spatial features [36]. Classical feature extraction methods include principal component analysis (PCA) [38]–[40], minimum noise fraction (MNF) [41] and independent component algorithm (ICA) [42], [43]. Nevertheless, these methods easily yield noisy visual performance, since the spatial information is not considered. To alleviate this issue, scholars have developed many spectral-spatial feature extraction methods. For example, Benediktsson *et al.* constructed extended morphological profiles (EMPs) by cascading a series of opening and closing operations [44]. Rasti *et al.* raised an orthogonal total variation component analysis to smooth image details, where a low-rank model was used to constrain the spectral dimension [45]. Duan *et al.* developed a structural profile to extract discriminative features of HSIs, which has strong robustness to image noise [46]. Zhang *et al.* proposed superPCA method to extract global and local spectral-spatial features [47].

Classifiers aim to assign category labels to the pixels of a given data [48], including spectral classifiers and spectral-spatial classifiers. Spectral classifiers are performed on the raw data to get classification results, such as support vector machine (SVM) [49], [50], decision tree (DT) [51], [52], and random forest (RF) [53]. However, these spectral classifiers cannot obtain satisfactory classification accuracy. In recent years, many spectral-spatial classifiers have been investigated, including mathematical morphology-based spectral-spatial classifiers, sparse representation-based classifiers, and deep learning-based spectral-spatial classifiers. The mathematical morphology-based spectral-spatial classifiers aim at designing a spectral-spatial classification framework by fusing

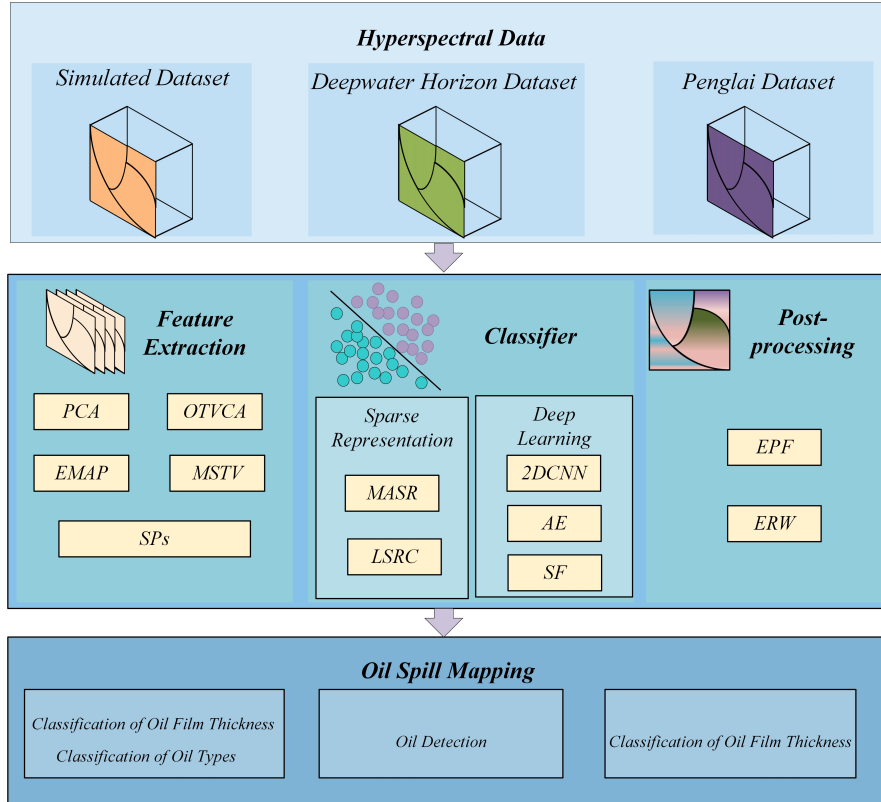


Fig. 1. General workflow for hyperspectral oil spill mapping.

different levels or types of features. For example, Nicola *et al.* proposed ICA-based morphological attribute profiles followed by an SVM classifier [54]. Li *et al.* developed a subpixel-pixel-superpixel-based multi-view active learning classification method, in which a disagreement correlation among different views and a posterior probability prediction were utilized to extend training samples [55]. The sparse representation-based classifiers are to construct a discriminative dictionary, and minimize the distance between the test samples and its approximation from each class to determine the class label. For instance, Fang *et al.* proposed the multi-scale sparse representation technique to adaptively extract useful information for the classification of HSIs [56]. Fu *et al.* designed a shape-adaptive sparse representation model, where a superpixel segmentation method was used to construct shape-adaptive regions. The deep learning-based spectral-spatial classifiers aim at extracting high-order semantic information followed by a multilayer perceptron to obtain classification results [48]. For example, Hang *et al.* proposed a two-layer recurrent neural network (RNN) to decrease the redundant and complementary information of HSIs. Zhu *et al.* designed a spectral attention module (SeAM) and a spatial attention module (SaAM) to improve the characterization ability of HSIs [57].

The post-processing methods use the correlation among adjacent pixels to remove the noisy labels. Representative post-processing classification methods include Markov random fields (MRF), edge-preserving filtering (EPF), and extended random walker (ERW). For example, Pedram *et al.* proposed a hidden MRF method for spectral-spatial classification of

HSIs, in which the MRF model was used to optimize the class probability [58]. Kang *et al.* presented an EPF-based post-processing method to improve the classification performance of homogeneous regions [59]. Kang *et al.* used the ERW method to encode the spatial dependencies of HSIs with a weighted graph [60].

The presented studies exhibit the huge potential of advanced machine learning methods for land cover mapping. However, it is not clear whether these methods can effectively identify different types of oil films or which one can achieve the best classification performance for oil spill mapping. In this paper, we compare the classification performance of several representative classification approaches (e.g., feature extraction, classifier, and post-processing-based methods) using three case studies. The case studies are comprised of a simulated dataset acquired from an outdoor experiment and two real oil spill accidents that cover different challenges with regard to oil spill characteristics, imaging scenes, and sensors. In all three examples, twelve different classification approaches are selected to evaluate the performance of oil spill mapping in terms of both detection capability and computational efficiency.

The rest of this work is organized as follows. Section II depicts the datasets used in the experiments. Section III presents the used methods in this work. Section IV is devoted to the experiments and results. Section V discusses the influence of different factors. Finally, Section VI presents the conclusions of this work.

II. DATASETS

A. Simulated dataset

The outdoor experiment was implemented in Qingdao Scientific Research Base, China on September 21, 2020. A large experimental pool with 50 m long, 40 m wide, and 2 m deep was constructed near the coast of the Yellow Sea. The location and overhead view of the experimental pool were shown in Fig. 2. In the outdoor experiment, hyperspectral oil spill images were obtained by a Nano-Hyperspec sensor installed on a DJI-M600PRO UAV. The Nano-Hyperspec sensor uses the push broom mode to capture the simulated dataset. The details of the Nano-Hyperspec and the DJI-M600PRO UAV are listed in Table I.

To better explore the potential of HSIs for identifying different types of oil spills and different thicknesses of oil films, we built nine enclosures with Polyvinyl Chloride (PVC) boards. Each enclosure was 1m long, 1m wide, and 1.3m height. In addition, in order to prevent the oil from leaking to the nearby Yellow Sea, an oil containment boom was placed around the enclosures. In the outdoor experiment, crude oil, gasoline, palm oil, fuel oil, and diesel were selected as research materials of different oil films. Additionally, we set the crude oil (1.5 mm, 2.5 mm, and 3.5 mm) and fuel oil (1.0 mm and 2.0 mm) to explore the performance of different thickness levels of oil films. After even spread of oil films, the Nano-Hyperspec loaded by DJI-M600PRO UAV captured the HSIs in sunny weather. The detailed information of the simulated dataset is shown in Table II. The visualization of the dataset and ground truth is shown in Fig. 3.

TABLE I
DETAILS OF NANO-HYPERSPEC SENSOR AND DJI-M600PRO UAV.

	Parameters	Indexes
Nano-Hyperspec	Wavelength range	400-1,000 nm
	Spectral bands	270
	Camera technology	CMOS
	FWHM Slit Image	6 nm
DJI-M600PRO	Maximum horizontal flight speed	65 km/h
	Maximum load	15.5 kg
	Maximum ascent/descend speed (m/s)	5/3 m/s

TABLE II
DETAILS OF THE SIMULATED DATASET.

Images	Captured height	Resolution	Fight time	Solar altitude angle
A01	40m	0.025m	09:21	36°51'
A02	35m	0.022m	10:21	47°42'
A03	35m	0.022m	10:40	49°54'
A04	35m	0.022m	11:11	52°40'
A05	35m	0.022m	11:40	54°09'
A06	35m	0.022m	13:08	50°52'
A07	35m	0.022m	14:18	40°47'

B. Penglai dataset

On 4 June 2011, an oil spill accident occurred in the Penglai 19-3 oil field, which led to massive crude oil and oil-based mud into the ocean. This accident polluted around 6,200 square kilometers of ocean area [61], [62]. The site of Penglai 19-3 oilfield platform as shown in Fig. 4. The

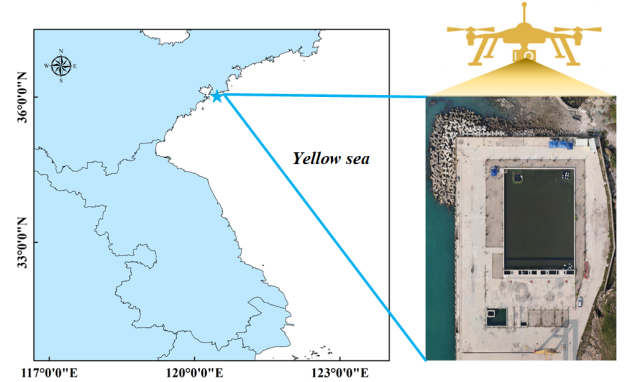
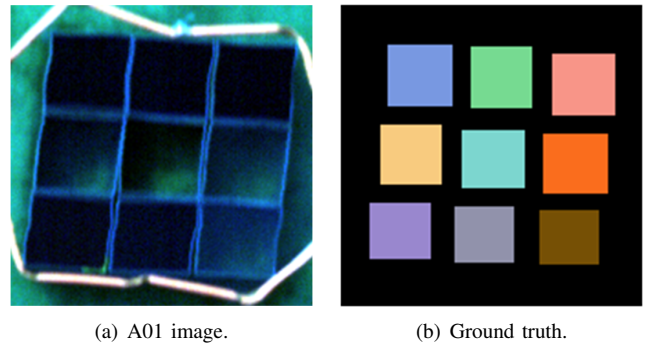


Fig. 2. Outdoor experimental site.



(a) A01 image. (b) Ground truth.
Legend:
■ Crude oil 1.5mm ■ Crude oil 2.5mm ■ Crude oil 3.5mm ■ Gasoline ■ Sea water
■ Palm oil ■ Fuel oil 1.0mm ■ Fuel oil 2.0mm ■ Diesel

Fig. 3. Simulated dataset.

Penglai oil spill dataset was obtained by the AISA+ hyperspectrometer (Finland, Specim company) loaded on a sea surveillance aircraft. This dataset has 258 spectral channels ranging from 400 to 1,000 nm with the spectral resolution of 5 nm. The study area contains 450×800 pixels. It should be mentioned that this dataset is contaminated by sun glint. Accordingly, it is difficult to detect oil spill areas for all considered methods. As shown in Fig. 5, the imaging scene contains oil spill, seawater, working ships, and shadow.

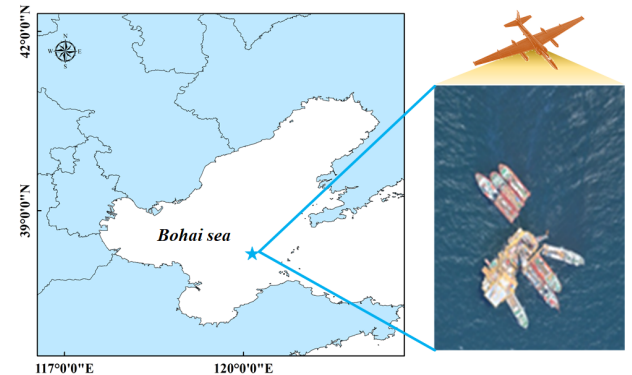


Fig. 4. The site of Penglai 19-3 oilfield platform.

C. Deep water horizon dataset

On April 20, 2010, an oil drilling platform named Deepwater Horizon (DWH) operated in the Gulf of Mexico (Fig. 6)

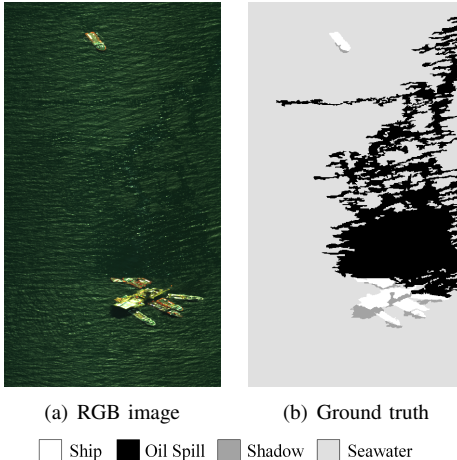


Fig. 5. Penglai dataset.

exploded. The accident resulted in the death of 11 workers and was the most serious oil spill accident in history. As a result, about 319 million barrels of oil spilled into the ocean [63], covering an area of more than 20,000 square kilometers [64], [65]. National aeronautics and space administration jet propulsion Laboratory (NASA JPL) used an airborne visible infrared imaging spectrometer (AVIRIS) to collect HSIs. AVIRIS is the first solar reflectance imaging spectrometer in this world invented by JPL with 224 spectral bands from 400 nm to 2,500 nm [66]. Two acquired HSIs are named B01 and B02 with the size of 350×500 pixels. It can be seen that oil spills in the dataset have different types of states due to weathering and emulsification [67].

Bonn Agreement [68] defines the oil film thickness as five categories as shown in Table III according to the visual appearance of oil in a small area. However, due to the low spatial resolution of AVIRIS, a pixel may contain different thicknesses of oil film. There are three classes of thickness $< 50\mu\text{m}$ in the Bonn Agreement, but thickness $< 25\mu\text{m}$ were not detected by Tetracorder (Software developed by USGS to process AVIRIS data) [69]. Moreover, pixels with thickness $> 200\mu\text{m}$ are only 5% of the total number of pixels, but contain more than 45% of the total oil volume [70]. Therefore, according to [70], the Bonn Agreement is modified to three oil film thicknesses as shown in Table III. The visualization of the dataset and ground truth is shown in Fig. 7.

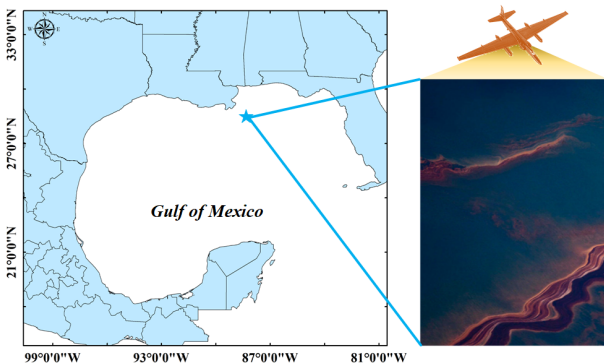


Fig. 6. The location of DWH platform.

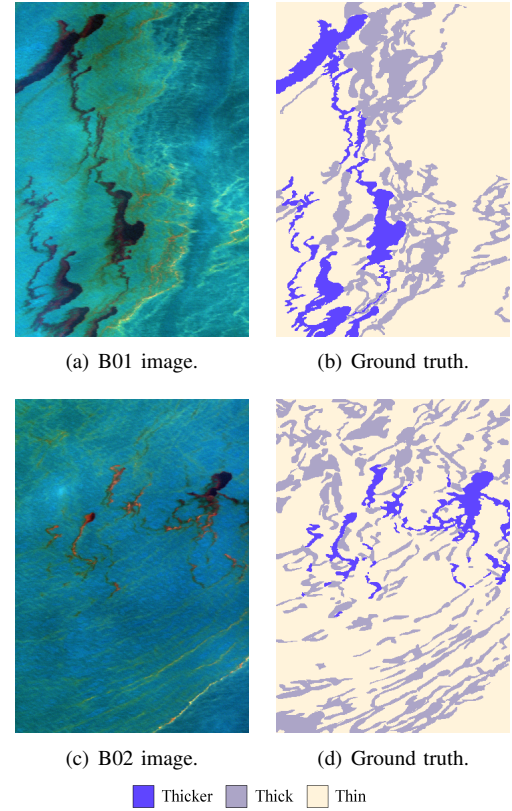


Fig. 7. DWH dataset.

III. METHODOLOGY

A. Feature extraction methods

Due to the high spectral dimension, HSI holds a large amount of redundant information. Feature extraction is an effective technique to extract discriminative spectral-spatial features and decreases the number of spectral dimension. Here, several classical and representative feature extraction methods are adopted to assess the performance of oil spill mapping.

1) *PCA*: As a classical and unsupervised feature extraction (UFE) technique, PCA and its variants have been widely applied for HSIs [71], [72]. PCA algorithm transformed high-dimensional raw data into a low-dimensional space by using a multivariable linear transformation. First, the HSI has converted to a data matrix \mathbf{I} after doing zero-mean. Then, the eigenvector and corresponding eigenvalue are computed as follows:

$$\mathbf{C} = \mathbf{V}\mathbf{E}\mathbf{V}^T \quad (1)$$

where \mathbf{C} means the covariance matrix of \mathbf{I} . \mathbf{V} is the eigenvector. \mathbf{C} is the eigenvalue. The first three principal components are selected to construct image features.

2) *Extended multi-attribute profiles (EMAP)*: EMAP aims to extract the spectral-spatial features with mathematical morphology operation [73]. First, the ICA is used to reduce the number of spectral dimension. Then, the attribute profile (AP) of each component according to Eq. (2) is calculated and combined into the extended morphological attribute profile (EAP).

$$EAP = \{AP(FR_1), AP(FR_2), \dots, AP(FR_c)\} \quad (2)$$

TABLE III
THE BONN AGREEMENT AND THICKNESS CLASSIFICATION IN THIS STUDY

Bonn Agreement classes			This study	
Code	Appearance	Layer thickness(μm)	Class	Layer thickness(μm)
1	Sheen	0.04-0.3		
2	Rainbow	0.3-5.0	Thin	≤ 50
3	Metallic	5.0-50		
4	Discontinuous true color	50-200	Thick	50-200
5	Continuous true color	> 200	Thicker	> 200

where FR_C means C th feature after ICA. AP is calculated as Eq. (3):

$$AP(\mathbf{L}) = \{\phi_n^T(\mathbf{L}), \phi_{n-1}^T, \dots, \phi_1^T(\mathbf{L}), \mathbf{L}, \gamma_1^T(\mathbf{L}), \dots, \gamma_{n-1}^T(\mathbf{L}), \gamma_n^T(\mathbf{L})\} \quad (3)$$

where ϕ^T refers to morphological attribute thickening operators. γ^T refers to attribute thinning operators. \mathbf{L} means the grayscale image. T means the criterion. EMAP is constructed by the stacked vector approach (SVA), which effectively integrates the global effective feature information.

3) *Orthogonal total variation component analysis (OTVCA)*: In [45], OTVCA is a dimension reduction method based on the low-rank model, in which the features of the raw data are calculated by solving the total variation penalized least squares problem in Eq. (4).

$$\begin{aligned} (\hat{\mathbf{F}}, \hat{\mathbf{V}}) = \arg \min_{\mathbf{F}, \mathbf{V}} J(\mathbf{F}, \mathbf{V}) &= \arg \min_{\mathbf{F}, \mathbf{V}} \frac{1}{2} \left\| \mathbf{Y} - \mathbf{F}\mathbf{V}^T \right\|_F^2 \\ &+ \lambda \sum_{i=1}^r \left\| \sqrt{(\mathbf{D}_h \mathbf{f}_{(i)})^2 + (\mathbf{D}_v \mathbf{f}_{(i)})^2} \right\|_1 \end{aligned} \quad (4)$$

where \mathbf{F} indicates extracted features. \mathbf{V} represents the basis matrix. \mathbf{Y} stands for vectorized original image in matrix form. \mathbf{D}_h is the operator of first-order vertical, and \mathbf{D}_v is the operator of first-order horizontal. $\mathbf{f}_{(i)}$ means vectorized feature of i -th column of \mathbf{F} .

4) *Multi-scale total variation (MSTV)*: MSTV is an effective feature extraction method, which can well eliminate the image noise and increase the spectral variability of different ground objects [46]. First, an averaging method is used to reduce the number of spectral dimension. Then, a relative total variation (RTV) is used to construct the multi-scale structural features of the dimension-reduced data, which can effectively reduce useless information such as redundant texture and noise. Finally, KPCA is adopted to fuse the multi-scale structural features. The structural features are estimated as follows:

$$\arg \min_{\mathbf{S}} \sum_{i=1}^T (\mathbf{S}_i - \mathbf{I}_i)^2 + \lambda \cdot \left(\frac{\mathcal{D}_x(i)}{\mathcal{L}_x(i) + \varepsilon} + \frac{\mathcal{D}_y(i)}{\mathcal{L}_y(i) + \varepsilon} \right) \quad (5)$$

where \mathbf{I} means the input HSI, and \mathbf{S} means the output structural image. T indices the number of all pixels. λ and ε are the free parameters controlling the smoothness of structural features and preventing division by zero, respectively. \mathcal{D}_x and \mathcal{L}_x are the windowed total variations and the inherent variations in the x-direction, while \mathcal{D}_y and \mathcal{L}_y are the windowed total variations and inherent variations in the y-direction. More

details can be referred to [46], [74]. In this way, this method not only ensures that the structural features retain the effective information of the original data as much as possible, but also confirms that invalid noise and texture are removed.

5) *Structural profiles (SPs)*: The SPs method is intended to retain the main geometrical information and smooth out useless details [75]. The hyperspectral image is modeled as a combination of the structural profile and the texture profile. An adaptive texture smoothing model is designed to extract the significant structural component, and the split Bregman iteration algorithm is used to solve this novel model. The specific model is shown as follows:

$$\arg \min_{\mathbf{S}} \|\mathbf{S} - \mathbf{I}\|_2^2 \odot \omega + \lambda \|\mathbf{S}\|_{TV} \quad (6)$$

where \mathbf{I} means the dimension reduced data. \mathbf{S} is structural profile. ω controls the similarity of pixel neighborhood. λ means a free parameter. The specific solution steps and detailed explanation are given in [75].

B. Classifier

Sparse representation is a classic tool in the field of signal processing, and it has been widely used in all kinds of aspects such as image restoration [76], image classification [56], and image super-resolution [77]. The raw signal is viewed as a linear combination of several atoms [78], which has been also applied in land cover mapping, image super-resolution [79], target detection [80] and image denoising [81].

1) *Multi-scale adaptive sparse representation (MASR)*: Fang *et al.* proposed a MASR method for material identification [56]. Specifically, one structural dictionary \mathbf{D} and the multi-scale matrix $\mathbf{Y}^{\text{multi-scale}}$ are first constructed. Second, in order to employ the correlations among multi-scales, MASR designs a new norm $\ell_{\text{adaptive},0}$ to represent a multi-scale sparse coefficients matrix $\mathbf{A}^{\text{multiscale}}$ as Eq. (7). Third, the sparse coefficients are obtained by iteration.

$$\begin{aligned} \hat{\mathbf{A}}^{\text{multiscale}} &= \arg \min_{\mathbf{A}^{\text{multiscale}}} \|\mathbf{Y}^{\text{multiscale}} - \mathbf{D}\mathbf{A}^{\text{multiscale}}\|_F \\ \text{subject to } &\|\mathbf{A}^{\text{multiscale}}\|_{\text{adaptive},0} \leq K. \end{aligned} \quad (7)$$

where $\mathbf{A}^{\text{multiscale}}$ is the multiscale sparse matrix and $\mathbf{Y}^{\text{multiscale}}$ is a multiscale matrix. \mathbf{D} indicates a structural dictionary. K means an upper limit of a given sparsity level. Compared with other sparse expression methods, MASR is more accurate in terms of edges and details because of introducing multi-scale information.

2) *Locality-constrained sparse representation classifier (L-SRC)*: Zhang *et al.* constructed LSRC to improve the classification performance [82]. LSRC assumes that the euclidean distances between pixels of the same class are also close, so the k -nearest neighbor (KNN) algorithm is used to select more dominant atoms from the training samples. This design also reduces the computing complexity of the sparse representation model. To enhance the data separability, Linear Discriminant Analysis (LDA) is used to map the data to a low dimension space. As shown in Eq. (8), it is the Euclidean distance d_n between a training sample \mathbf{x}_n and the testing sample \mathbf{y} in LDA projected space.

$$d_n = \|\mathbf{T}\mathbf{y} - \mathbf{T}\mathbf{x}_n\|_2^2 \quad (8)$$

where \mathbf{T} means the LDA mapping matrix.

Besides, deep learning has become a popular research topic in HSI classification, which can effectively extract high-order semantic information of the input [83]. Various deep learning models have been proposed for classification of HSIs. In the early stage, researchers proposed some shallow deep networks by using several convolutional layers and pooling layers to extract spatial, spectral, or spatial-spectral features. To improve the classification performance of HSIs, some advanced deep networks and frameworks have been also applied in hyperspectral image classification in recent years, such as self-attention mechanism, self-supervised learning and active learning. In this work, several representative and advanced deep learning classifiers are selected to test the oil spill detection performance.

3) *2D convolutional neural (2DCNN) network*: The 2DCNN was applied for land cover mapping [84]. Each layer in the framework is composed of a convolutional layer and a pooling layer. The value of each neuron can be computed as Eq. (9)

$$v_{ij}^{xy} = g \left(b_{ij} + \sum_m \sum_{p=0}^{P_i-1} \sum_{q=0}^{Q_i-1} w_{ijm}^{pq} v_{(i-1)m}^{(x+p)(y+q)} \right) \quad (9)$$

where v_{ij}^{xy} means the value at (x,y) of the j th channel in the i th layer. w_{ijm}^{pq} is the value of weight (p, q) connected to the m th channel. P_i is the height of convolution kernel and Q_i is the width of convolution kernel. b_{ij} represents the bias.

4) *Autoencoders (AE)*: AE is a representative unsupervised learning network model including two main structures: encoder and decoder. A simple AE includes one visible layer, one hidden layer, one reconstruction layer, and an activation layer. The encoder maps the input matrix to the hidden layer as Eq. (10), while the decoder converts the feature layers to an output layer as Eq. (11).

$$\mathbf{Y} = f(\mathbf{W}_1 \mathbf{Z} + \mathbf{b}_1) \quad (10)$$

$$\hat{\mathbf{Z}} = f(\mathbf{W}_2 \mathbf{Y} + \mathbf{b}_2) \quad (11)$$

where \mathbf{Z} is the input data. \mathbf{Y} is the latent feature. $\hat{\mathbf{Z}}$ is the reconstruction result. \mathbf{W}_1 and \mathbf{W}_2 are the weights. \mathbf{b}_1 and \mathbf{b}_2 are the biases.

5) *SpectralFormer (SF)*: In recent years, the transformer [85] structure applied to natural language processing has attracted widespread attention and successfully developed to image processing [86], [87]. It has been proved that the self-attention mechanism can better extract the global information of data features. The self-attention mechanism can be formulated as Eq. (12).

$$z = \text{Attention}(Q, K, V) = \text{softmax}\left(\frac{QK^T}{\sqrt{d}}\right)V \quad (12)$$

where Q , K and V mean vectors generated from input data. The specific explanations and solutions can be referred to [85]. Hong *et al.* applied the transformer model to HSI classification, called SF [88]. SF utilizes the Vision Transformer (ViT) -based baseline network for HSIs. Transformer proved that the multi-head attention mechanism can better extract the global information of data features. In order to more focus on the spectral discrepancies and information connectivity, SF includes a group-wise spectral embedding (GSE) module and a cross-layer adaptive fusion (CAF) module. The former finely captures the local spectral signatures modeled as Eq. (13), while the latter fuses the information between layers modeled as Eq. (14).

$$\hat{\mathbf{A}} = \mathbf{WX} \quad (13)$$

$$\hat{z}^{(l)} \leftarrow \ddot{w} \begin{bmatrix} z^{(l)} \\ z^{(l-2)} \end{bmatrix} \quad (14)$$

where \mathbf{A} means the matrix of feature embeddings. \mathbf{W} is the matrix of linear transformations. \mathbf{X} is the matrix of spectral signatures. $\hat{z}^{(l)}$ is the fused operation in the l th layer. z means the feature. \ddot{w} is the parameter to control fusion.

C. Post-processing methods

1) *EPF*: Kang *et al.* proposed a simple yet effective HSIs classification framework with an edge-preserving filtering method [89]. The core idea is to optimize the probability map of each class by considering the correlation in the local regions. Further, the SVM classifier is first performed on the original data to obtain the probability map of each class, and then, the guided filtering (as shown in Eq. (15) is used to remove the scatter pixels.

$$\mathbf{O}_i = \frac{1}{K_i^b} \sum_{j \in \omega_i} G_{\delta_s}(\|i - j\|) G_{\delta_r}(|\mathbf{I}_i - \mathbf{I}_j|) \mathbf{P}_j \quad (15)$$

$$\mathbf{O}_i = a_i \mathbf{I}_i + b_j, \quad \forall i \in \omega_j. \quad (16)$$

In Eq. (15) \mathbf{O} is the filtered output image. \mathbf{I} is the guidance image. \mathbf{P} represents the n -th input image. i and j are respectively the i th, j th pixel. ω means a local window. $G_{\delta_s}(\|i - j\|)$ and $G_{\delta_r}(|\mathbf{I}_i - \mathbf{I}_j|)$ are gaussian decreasing functions. δ_s defines the size of local window. δ_r controls the weight of a pixel decreases. K^b is a normalizing term as Eq. (17).

$$K_i^b = \sum_{j \in \omega_i} G_{\delta_s}(\|i - j\|) G_{\delta_r}(|\mathbf{I}_i - \mathbf{I}_j|) \quad (17)$$

In Eq. (16), a_j and b_j are coefficients got by Eq. (18), ω is the parameter that controls the level of filtering blur.

$$E(a_j, b_j) = \sum_{i \in \omega_j} ((a_j \mathbf{I}_i + b_j - \mathbf{P}_i)^2 + \epsilon a_j^2) \quad (18)$$

This classification framework uses the gray image or the color image selected from the original image as the guide image to perform EPF on the classified probability map, which verifies that the local spatial structure information still has a strong improvement effect on the classification accuracy.

2) *ERW*: ERW is a graph model-based post-processing method that aims to optimize the classification map obtained by the spectral classifier. In more detail, the probability map is first obtained by using the SVM classifier. Then, the first principal component (PC) of HSIs with PCA constructs the weighted graph $G = (V, E)$. V represents pixels in the first PC, and E represents the edges of the first PC. Finally, the ERW is used to optimize the probability map by minimizing the energy function as Eq. (19).

$$\begin{aligned} E_{aspatxal}^n(\mathbf{p}_n) &= \mathbf{p}_n^T \mathbf{L} \mathbf{p}_n \\ &+ \sum_{q=1, q \neq n}^N \mathbf{p}_q^T \boldsymbol{\Lambda}_q \mathbf{p}_q + (\mathbf{p}_n - 1)^T \boldsymbol{\Lambda}_n (\mathbf{p}_n - 1) \end{aligned} \quad (19)$$

where \mathbf{p}_n indices the probabilities. \mathbf{L} means a sparse Laplacian matrix, and the specific solution method is described in [60]. $\boldsymbol{\Lambda}_n$ is a diagonal matrix and each element on the diagonal is the initial probability of pixels.

IV. EXPERIMENTS

In order to examine the detection performance of different classification approaches for oil spill mapping, twelve representative classification methods are adopted, including five feature extraction methods (i.e., PCA [90], EMAP [73], OTVCA [45], MSTV [46], SPs [75]), two sparse representation classification methods (i.e., MASR [56], LSRC [82]), three deep learning classification methods (i.e., 2DCNN [84], AE [91], SF [85]), and two post-processing methods (i.e., EPF [89], ERW [60]). These methods are highly cited publications and classical techniques in hyperspectral image classification community. Three widely used objective indexes are used to evaluate the classification performance, i.e., average accuracy(AA), overall accuracy (OA) and kappa coefficient (Kappa). For the training set, 1% samples are randomly selected from the reference image.

A. Parameter setting

In this section, the parameter settings of all methods follow the original method. Furthermore, we will provide a toolbox¹. All experiments are done on a computer with 64GB and a RAM intel (R) Core (TM) i9-10850K CPU and NVIDIA GeForce RTX 3090 GPU. Feature extraction, post-processing, and sparse representation are implemented computationally on MATLAB R2018a, while the deep learning models are implemented on the PyTorch platform.

¹https://github.com/PinkSlime/HSI_oil_spill_mapping

1) PCA: The number of principal components is the number of classes.

2) EMAP: EMAP method is a representative feature extraction technique [73]. The threshold values of α (area of regions) are set as 200,500 and 1000. The threshold values of δ (standard deviation) are set to be 2.5, 5, 7.5 and 10.

3) OTVCA: Three parameters are involved in OTVCA [45]. The number of extracted features is set to 16. The parameter which controls the level of smoothness is set as 0.01. The iteration is set as 200.

4) MSTV: In [46], the parameters that control the degree of smoothness are set to 0.003, 0.02, and 0.01. The parameters that control the maximum size of texture elements are set to 2, 1, and 3.

5) SPs: There are four parameters in SPs [75]. The weight of fusion is 0.5. The number of features after dimension reduction is 30. The smoothing parameter is set to 1.2. The number of kernel principal components is set to 40.

6) MASR: In this experiment, the multi-scale patch sizes are set to 3, 5, 7, 9, 11, 13, and 15 [56].

7) LSRC: There are two parameters in the LSRC algorithm [82]. The sparsity level is 6 and the number of nearest neighbors is set to 20.

8) 2DCNN: The CNN consists of three blocks. Each block includes a convolution layer, a batch normalization layer, an activation layer, and a pooling layer. The convolutional kernels of three convolutional layers are set to $3 \times 3 \times 32$, $3 \times 3 \times 64$, and $3 \times 3 \times 128$. The patch size, batch size, epoch, and learning rate of 2DCNN are set to 16, 128, 200, and 0.001, respectively.

9) AE: For AE [92], The encoder has three fully connected layers with the number of neurons of 32, 64, and 128, respectively. Similarly, the decoder has three fully connected layers with the number of neurons of 64, 32, and 32. The batch size, epoch, and learning rate of AE are set to 128, 200, and 0.001, respectively.

10) SF: The network framework of SF is based on ViT [88]. There are five cascaded encoder blocks. Each block includes a four-head Self-attention layer, a multilayer perceptron, and a nonlinear activation layer. The batch size, epoch, and learning rate of SF are set to 64, 500 and 0.0005.

11) EPF: There are two parameters in the EPF based guided filter [89]. The filtering size is fixed to be 3. The value of blur degree is set to 0.01.

12) ERW: The optional weighting parameter of the random walker is 710. The seed points are the pixel points of the training set [60].

B. Simulated dataset

The first case is studied on the simulated dataset. Fig. 8(a) shows the spectral reflectance of different thicknesses of crude oils. It can be observed that the difference between different thicknesses of oil films is very small. Fig. 8(b) gives the spectral difference of different fuel oils. Accordingly, it is challenging to distinguish them by different classification methods.

Fig. 9 shows the oil spill classification results of different methods on the A01 image. The PCA method yields a very

noisy oil spill classification map, and different thicknesses of crude oils cannot be distinguished. The EMAP method improves the classification visual effect compared to the PCA method. However, it cannot produce satisfactory classification performance for some oil films, such as Gasoline and Palm oils. For the OTVCA method, it is unable to accurately identify different thicknesses of crude oils. The MSTV method greatly improves the oil spill classification performance. Nevertheless, the crude oils with 2.5 mm and 3.5 mm are not well identified. The FDSI method achieves a satisfactory visual classification map. The MASR method yields an obvious block misclassification result. The LSRC method obtains a similar classification result to the PCA method. The 2DCNN method cannot well identify the crude oils with 1.5 mm and 2.5 mm. The AE method produces unsatisfactory classification performance in identifying different types of oil films. The SF method cannot work well in distinguishing different thicknesses of crude oils. The EPF method yields unsatisfactory classification performance in identifying different oil films. For the ERW method, different types of oil films are well distinguished.

Table IV shows the objective indexes of different oil spill classification methods on the simulated dataset. For feature extraction methods, the PCA-based feature extraction method obtains unsatisfactory objective accuracies while the SPs method obtains the highest classification accuracies among all feature extraction techniques. For sparse representation methods, the MASR and LSRC methods produce poor classification results compared to other types of classification techniques. Among all deep learning-based methods, the AE fails to obtain satisfactory objective results in terms of OA, AA, and Kappa coefficient. The 2DCNN method yields the highest objective accuracies among the three deep learning methods. For post-processing methods, the ERW produces the best classification performance. This is due to the fact that the correlation among neighboring pixels is fully considered by a graph model. In general, the feature extraction methods can better identify different types of oil films.

Furthermore, it can be observed that these classification methods can work well in identifying different thicknesses of fuel oils. On the contrary, most of them cannot effectively distinguish different thicknesses of crude oils even under ideal imaging conditions (e.g., solar altitude angle of 54°09', A05 Image). The difference in spectral profiles for three crude oils is very small, especially for 1.5 mm and 2.5 mm crude oils (see Fig. 8(a)). Different from the crude oils, the fuel oils with different thicknesses have significant differences in the wavelength ranging from 600 nm to 900 nm (see Fig. 8(b)), which can be regarded as feature channels.

C. Penglai dataset

The Penglai dataset, which is captured from a real accident scene, can better show the performance of different algorithms. Table V shows the objective indexes of different methods on the Penglai dataset, in which the best result is highlighted in bold. For feature extraction methods, the PCA method produces the lowest classification accuracies, since this feature extraction technique only considers the spectral information

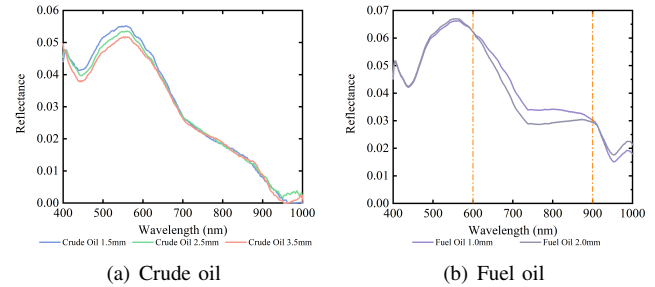


Fig. 8. The spectral curves of different oil films.

in the original image. The EMAP-based feature extraction method obtains the highest classification performance. For sparse representation methods, both the MASR and LSRC methods fail to work well in classifying different types of objects. For deep learning methods, the 2DCNN method can effectively detect the oil spill region in this dataset corrupted by sun glints among all studied methods. For post-processing classification methods, the ERW method produces the highest classification accuracies with respect to OA, AA, and Kappa coefficient. Generally, the ERW method still obtains satisfactory classification performance among all considered approaches for this case.

Besides, Fig. 10 shows visual results of different classification methods on the Penglai dataset. The PCA method cannot detect the oil spill region. The EMAP method boosts the classification method. However, there is salt-and-pepper noise in the oil spill region. For the OTVCA and MSTV methods, the oil spills are misclassified into seawater. The SPs method produces a noisy classification map for the oil spill and seawater classes. The MASR method cannot identify the oil spill region. The LSRC method also yields a very noisy classification result. The 2DCNN method can well remove the influence of sun glints in the oil spill region and better detect the oil spills. The AE and SF methods produce similar classification results in terms of visual maps. They can detect the oil spill area. However, the classification maps are still very noisy due to the influence of sun glints. The EPF and ERW methods can well remove the salt-and-pepper noise in the classification maps, since they can make full use of the spatial correlation among neighboring pixels. On the whole, the ERW method yields the best visual effect in identifying the four types of objects, i.e., ship, oil spill, shadow, and seawater.

D. DWH dataset

The third case is studied on the DWH dataset, i.e., B01 and B02 images. In this case, the oil spills have been spread with the movement of seawater, resulting in different thicknesses of oil spills, i.e., "thin" oil, "thick" oil, and "thicker" oil. Tables VI-VII shows the objective results of all studied approaches. For feature extraction methods, the PCA method still yields relatively low objective accuracies in this case. The SPs method obtains the highest OA, AA, and Kappa coefficient among all feature extraction techniques. For sparse representation methods, the LSRC method is still better than the MASR method in terms of OA, AA, and Kappa coefficient.

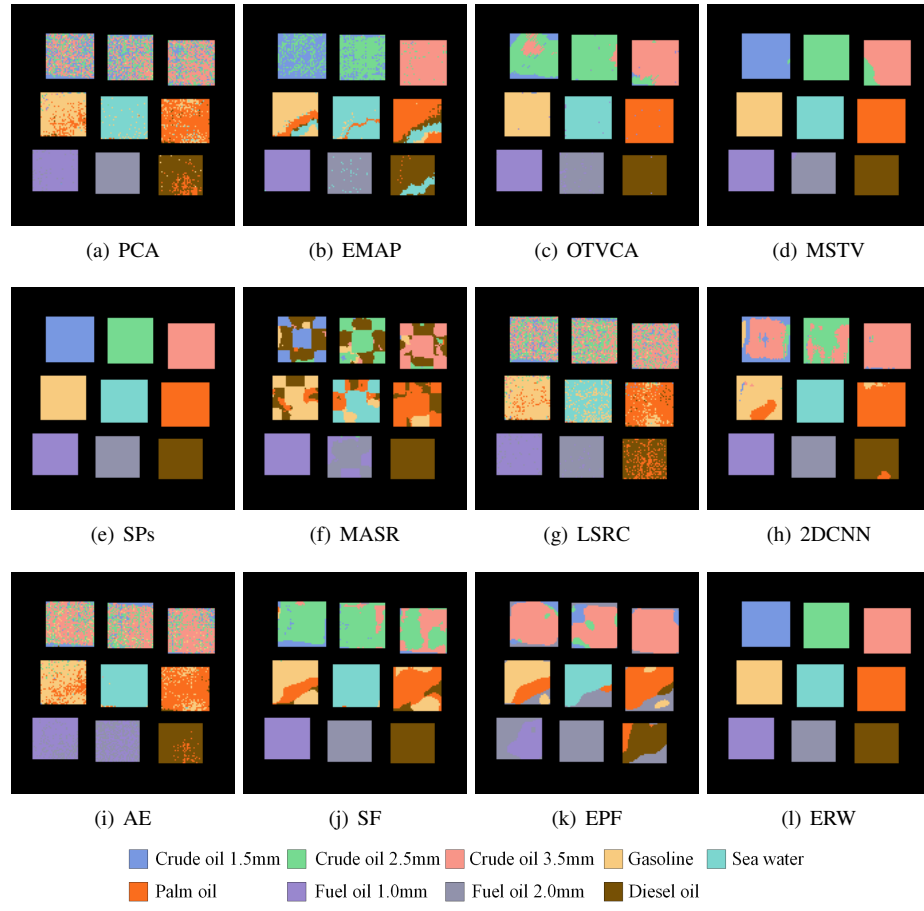


Fig. 9. Oil spill mapping results of different methods on A01 image.

TABLE IV
CLASSIFICATION ACCURACIES OF DIFFERENT METHODS IN PERCENTAGES FOR SIMULATED DATASET. THE BEST ACCURACY IN EACH ROW IS SHOWN IN BOLD.

	PCA	EMAP	OTVCA	MSTV	SPs	MASR	LSRC	2DCNN	AE	SF	EPF	ERW	
A01	OA	70.80	83.37	87.27	98.40	100	66.99	69.29	97.93	95.23	72.16	58.11	100
	AA	72.37	83.80	90.74	98.60	100	62.99	70.32	90.68	68.22	73.64	69.66	100
	Kappa	0.6712	0.8128	0.8568	0.9820	1	0.7993	0.6542	0.9160	0.8061	0.6869	0.5290	1
A02	OA	83.08	85.04	99.37	97.95	100	77.99	76.42	95.65	93.21	79.03	77.60	100
	AA	83.40	85.05	99.39	98.06	100	75.23	75.97	81.92	65.46	78.81	84.22	100
	Kappa	0.8097	0.8318	0.9929	0.9772	1	0.8226	0.7347	0.8561	0.7753	0.7641	0.7478	1
A03	OA	90.84	81.81	99.95	83.79	100	86.89	88.73	96.61	97.70	82.82	87.46	100
	AA	91.63	82.76	99.95	92.81	100	85.23	88.85	88.49	90.62	83.52	89.73	100
	Kappa	0.8969	0.7953	0.9995	0.8173	1	0.8892	0.8732	0.9058	0.9360	0.8069	0.8589	1
A04	OA	83.77	89.02	99.76	99.02	100	80.15	90.91	99.04	97.55	89.83	92.53	100
	AA	84.67	88.59	99.74	99.01	100	77.69	90.77	95.71	88.79	89.71	92.47	100
	Kappa	0.8173	0.8764	0.9973	0.9982	1	0.8239	0.8976	0.9718	0.9282	0.8856	0.9159	1
A05	OA	83.19	86.61	98.92	99.01	100	79.40	83.22	97.40	94.00	79.91	86.95	100
	AA	84.53	86.98	98.97	99.05	100	76.81	84.26	89.77	78.82	81.40	88.29	100
	Kappa	0.8107	0.8493	0.9878	0.9888	1	0.8095	0.8111	0.9278	0.8332	0.7741	0.8531	1
A06	OA	80.17	91.75	99.34	80.09	100	74.11	80.92	98.65	96.70	79.94	87.97	100
	AA	81.31	91.62	99.36	90.82	100	70.87	81.49	94.13	85.38	80.28	91.03	100
	Kappa	0.7768	0.9072	0.9926	0.7759	1	0.7691	0.7852	0.9614	0.9060	0.7744	0.8645	1
A07	OA	84.76	86.88	98.06	99.83	100	75.98	84.50	98.37	97.32	87.41	89.50	100
	AA	83.72	86.54	98.06	99.81	100	72.96	83.62	93.72	87.49	86.90	92.18	100
	Kappa	0.8284	0.8522	0.9782	0.9980	1	0.8085	0.8255	0.9554	0.9265	0.8583	0.8817	1

TABLE V
CLASSIFICATION ACCURACIES OF DIFFERENT METHODS IN PERCENTAGES FOR Penglai dataset. THE BEST ACCURACY IN EACH ROW IS SHOWN IN BOLD.

Class name	PCA	EMAP	OTVCA	MSTV	SPs	MASR	LSRC	2DCNN	AE	SF	EPF	ERW
Ship	86.62	94.95	93.30	93.71	95.26	80.14	88.71	86.50	90.37	87.16	93.92	94.19
Oil spill	41.56	77.39	78.20	75.34	77.55	45.01	67.63	88.53	83.85	73.40	79.24	79.82
Shadow	69.86	74.41	75.85	73.64	79.04	58.74	77.39	71.41	69.98	65.26	79.67	80.84
Seawater	95.39	96.21	94.23	92.69	95.79	99.08	95.25	95.01	93.42	96.81	97.75	97.83
OA	84.08	92.18	90.81	89.03	91.94	87.41	89.37	93.45	91.40	91.62	93.77	93.86
AA	73.36	85.74	85.40	83.85	86.91	70.74	82.25	85.36	84.40	80.66	87.64	88.17
Kappa	0.5017	0.7805	0.7488	0.7038	0.7742	0.5830	0.6945	0.8166	0.7571	0.7582	0.8226	0.8278

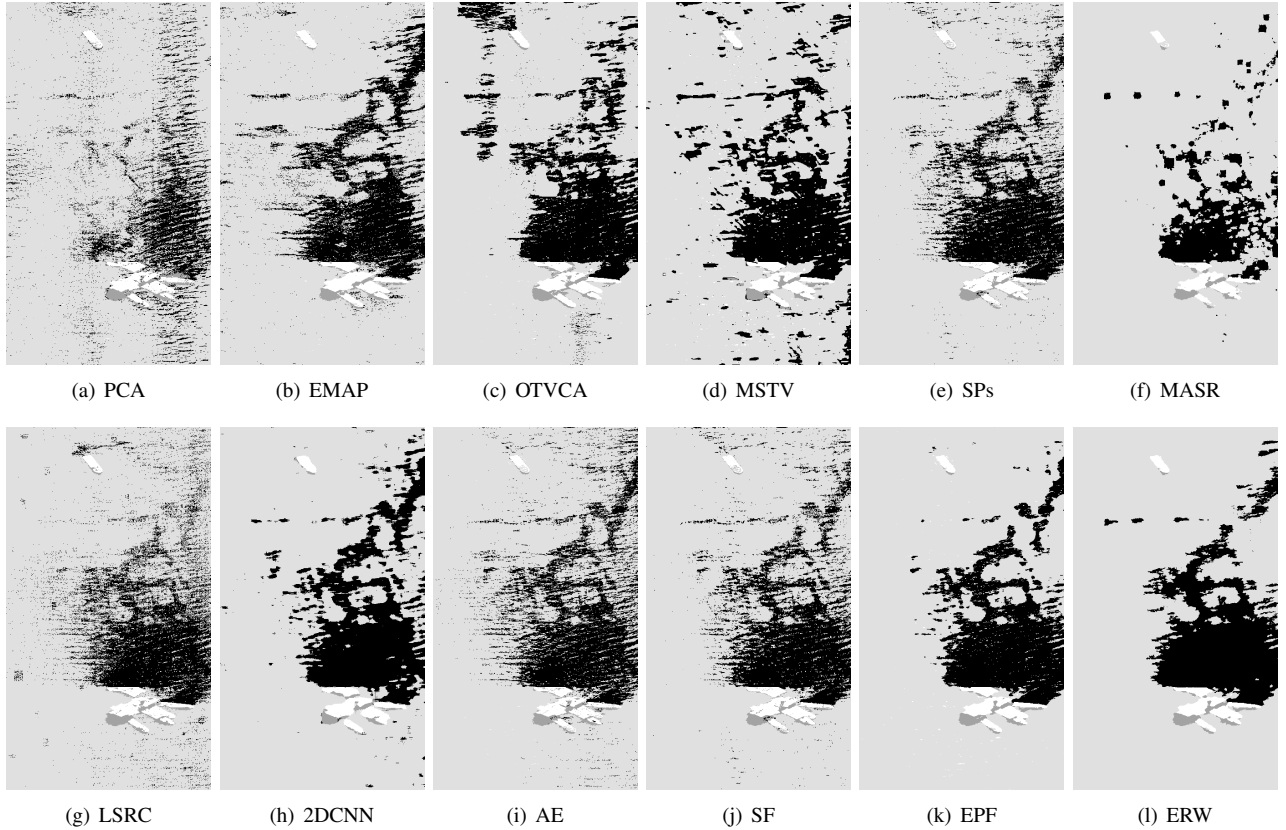


Fig. 10. Oil spill mapping results of different methods on Penglai dataset.

However, they cannot obtain superior classification accuracies. For deep learning methods, the AE method obtains the best classification performance on the DWH dataset. For post-processing methods, the ERW method also obtains relatively high classification accuracies in this case.

In addition, Fig. 11 shows the mapping results on the B01 image. It can be observed that the PCA method ignores the "thick" oil distribution, and produces many cluttered and scattered misclassified pixels. The EMAP and OTVCA methods misclassified the "thicker" oil into "thick" oil. The MSTV and EPF methods show the over-smoothing effect on the classification maps. The SPs, LSRC, AE, SF, and ERW methods present better classification maps. Similar to the previous cases, the MASR method still cannot obtain a satisfactory classification effect. It is worth noting that, unlike the previous cases, the 2DCNN method does not work well in this complex oil spill scene.

V. MODEL ANALYSIS

A. The potential of different types of methods

The experimental results clearly show the potential of different types of classification methods. Generally, the spectral-spatial classification methods are always better than the spectral-based classification methods, which illustrates the importance of using spatial correlation of neighboring pixels. For example, the OTVCA method is superior to the PCA method for all cases. In addition, variations of illumination due to imaging conditions and shadows during data acquisition are a challenging problem in oil spill mapping. Most classification methods suffer from performance degradation when the original image is corrupted by sun glint (see case 2).

This study also illustrates the differences in the classification effect of conventional machine learning and advanced deep learning methods. The use of conventional machine learning methods often leads to an over-smoothed phenomenon in the boundaries of different objects due to inappropriate

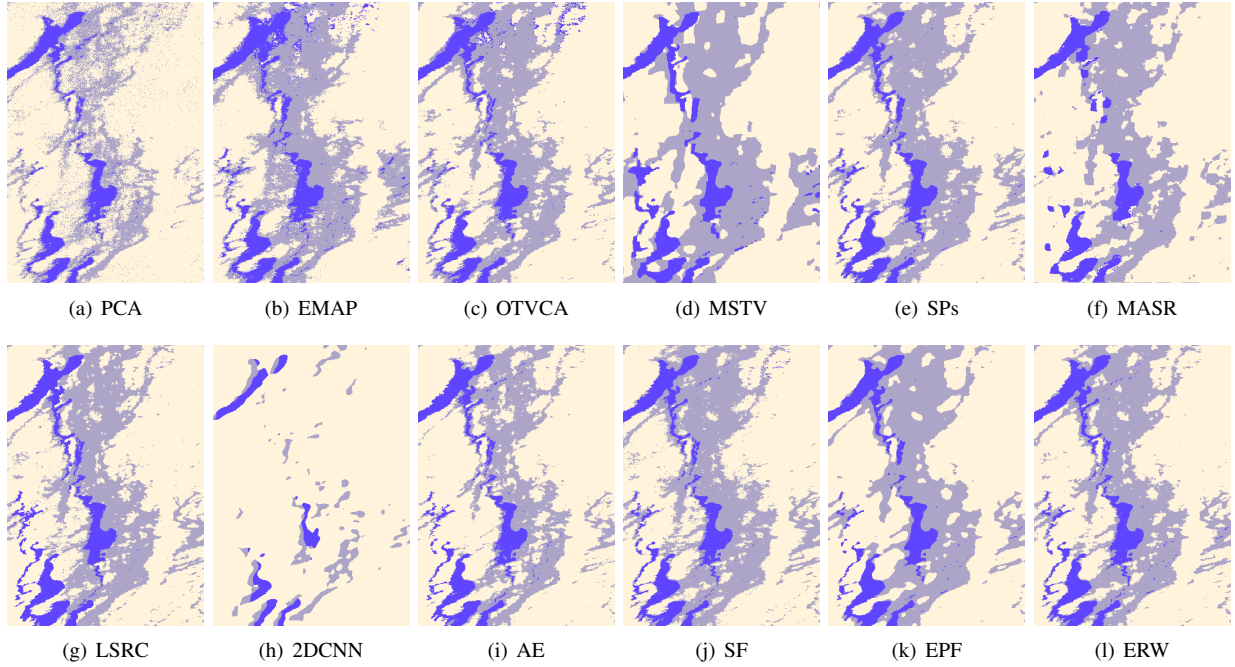


Fig. 11. Oil spill mapping results of different methods on B01 image.

TABLE VI

CLASSIFICATION ACCURACIES OF DIFFERENT METHODS IN PERCENTAGES FOR B01 IMAGE. THE BEST ACCURACY IN EACH ROW IS SHOWN IN BOLD.

Class name	PCA	EMAP	OTVCA	MSTV	SPs	MASR	LSRC	2DCNN	AE	SF	EPF	ERW
Thin	69.91	83.64	77.24	87.45	87.22	74.36	89.43	67.38	91.67	83.68	83.27	86.58
Thick	67.86	88.37	87.64	92.54	92.84	86.60	91.03	50.97	59.43	93.57	91.78	92.19
Thicker	87.13	73.41	80.30	74.55	78.90	82.12	81.05	97.11	94.87	76.62	80.24	79.20
OA	82.00	77.08	81.32	79.03	82.21	82.17	83.65	78.33	85.84	80.34	82.60	82.24
AA	74.97	81.81	81.73	84.85	86.92	81.02	87.17	71.81	81.99	84.63	85.10	85.99
Kappa	0.6015	0.5700	0.6270	0.6035	0.6516	0.6324	0.6725	0.5943	0.6966	0.6218	0.6538	0.6511

TABLE VII

CLASSIFICATION ACCURACIES OF DIFFERENT METHODS IN PERCENTAGES FOR B02 IMAGE. THE BEST ACCURACY IN EACH ROW IS SHOWN IN BOLD.

Class name	PCA	EMAP	OTVCA	MSTV	SPs	MASR	LSRC	2DCNN	AE	SF	EPF	ERW
Thin	57.88	73.38	58.50	84.96	72.35	39.04	72.19	54.35	89.34	67.47	66.74	71.29
Thick	11.88	80.58	79.83	74.63	79.89	53.49	78.57	61.77	60.70	71.22	69.53	74.95
Thicker	98.75	76.80	77.45	69.35	79.56	88.07	80.11	80.17	89.24	83.98	83.46	82.24
OA	76.58	77.50	77.03	71.58	79.27	77.57	79.35	76.33	81.84	80.18	79.38	80.00
AA	56.17	76.92	71.93	76.41	77.27	60.20	76.96	65.43	79.76	74.23	73.24	76.16
Kappa	0.2876	0.5368	0.5240	0.4501	0.5642	0.4416	0.5610	0.3817	0.5859	0.5585	0.5421	0.5678

parameters. Moreover, determining how to select the optimal parameter for different scenes is always a challenging problem for all machine learning algorithms. The deep learning-based classification methods avoid manual selection of feature extraction methods, which can smartly learn the deep features. By comparing the classification results of machine learning methods and deep learning methods, it is found that the machine learning methods not only outperform the deep learning methods but also exhibit very competitive in terms of classification performance with respect to deep learning methods.

Classification methods remain challenging when faced with oil films of varying thickness, which can be seen from the simulated dataset and DWH dataset. Compared with other methods, the ERW method performs well in all cases. The reason is that the ERW method makes full use of the spatial

correction of local pixels calculated by the graph model. Therefore, the ERW method is more suitable for oil spill mapping.

B. The influence of image noise

In this subsection, we analyze the influence of image noise on classification performance. Four representative methods, i.e., SPs, AE, LSRC, and ERW, are adopted since they obtain relatively good classification performance. An experiment is performed on the B01 image, in which each band is added by zero-mean Gaussian noise with different variances σ is set from 0.01 to 0.10 with step 0.01. Fig. 12 presents the objective results of the four considered methods. It is obvious that the classification performance of the ERW method gradually decreases as the noise level increases. Moreover, when $\sigma = 0.05$, the classification performance cannot acceptably. The AE and

LSRC methods tend to decrease when the original image is corrupted by image noise. By contrast, the SPs method is robust to image noise. The reason is that the feature extraction method models the hyperspectral image as the combination of the structural profile (intrinsic property, salient structure, etc.) and the texture profile (e.g., image noise, texture details, etc.).

C. The influence of different numbers of training samples

This subsection is to analyze the influence of different numbers of training samples. Fig. 13 gives the classification accuracies of four considered methods with different numbers of training samples, in which the number of training samples is from 10 to 100 with step 10 for each class. An experiment is performed on the B01 image. The training set is randomly selected from the ground truth, and each experiment is repeated ten times to reduce the influence of random selected strategy. The reported result is obtained by calculating the average of ten experiments. From this figure, several conclusions can be drawn. First, as the number of training samples increases, the classification accuracies of all methods tend to increase, especially for the ERW method. Second, the LSRC and AE methods still show satisfactory classification performance in the case of limited training samples. For example, when the number of training samples is 10, the LSRC method obtains OA=83.08%, AA=81.79%, and Kappa=0.6434, respectively. Third, as the number of training samples increases, the classification performance of SPs gradually surpasses other methods.

D. Computing time

Here, we discuss the processing time (in seconds) of all considered classification methods. Fig. 14 depicts the computing time of all methods on three datasets. Several key conclusions can be summarized: First, the computing time of the MASR method is very high, because it takes a lot of time to learn multi-scale dictionaries. Second, the computing time of deep learning methods takes more time than feature extraction methods. Third, the running time of the post-processing methods are moderate among all considered approaches since the post-processing operation is fast. It is worth noting that the computing time of the EMAP method is less than those of other methods for the first two datasets, but it takes longer time for the third dataset. The main reason is that the EMAP method extracts high-dimension spectral-spatial features from DWH dataset, which greatly increases the cross-validation time.

VI. CONCLUSIONS

HSI classification for oil spill mapping has been a hot topic in the remote sensing field. Most of the current oil spill mapping is limited to detecting a single type of oil species. In this work, we summarize various common methods for hyperspectral oil spill mapping. These methods mainly optimize three steps in the classification process, namely feature extraction, classifiers including sparse representation and deep learning, and post-processing. Three datasets, namely simulated dataset, Penglai dataset, and DWH dataset, are captured or collected to analyze the classification performance.

According to the experimental results, several key conclusions can be obtained:

1) The pixel-level feature extraction methods easily produce noisy classification maps. However, the edges of different oil films in the classification maps are more similar to the ground truth. The spectral-spatial feature extraction methods tend to yield over-smoothed classification results because of inaccurate parameter settings.

2) The oil spill mapping performance of sparse representation classifiers overly relies on the constructed dictionary. For example, the MASR method fails to obtain satisfactory performance for oil spill mapping in terms of computational burden and classification accuracies. The deep learning classifiers obtain competitive classification performance among all approaches when the number of training samples is relatively small. Moreover, the deep learning classifiers can automatically learn complex features from HSIs in an end-to-end manner, which has stronger adaptability for different ocean scenes.

3) The post-processing classification methods can obtain better classification performance when the input HSI is a strong geometric characteristics scene. This is used to the fact that this type of method fully utilizes the correlation among neighboring pixels.

4) Among all considered approaches, the structural profiles-based method has strong robustness to image noise, which is more suitable for oil spill HSIs corrupted by noise. The reason is that this method views the HSI as a combination of a structural profile (i.e., significant structures and features) and a texture profile (i.e., image noise and useless details), in which the structural profiles are fed into the spectral classifier.

In the future, it is important to develop some unsupervised, weakly supervised, or self-supervised classification methods for oil spill mapping so as to overcome the problem about lacking of the high-quality and high-amount of training samples. In addition, it is also necessary to develop novel lightweight oriented models deployed in the aircraft systems or orbiting satellites to achieve real-time oil spill mapping.

REFERENCES

- [1] B. Q. Huynh, L. H. Kwong, M. V. Kiang, E. T. Chin, A. M. Mohareb, A. O. Jumaan, S. Basu, P. Geldsetzer, F. M. Karaki, and D. H. Rehkopf, "Public health impacts of an imminent Red Sea oil spill," *Nature Sustainability*, vol. 4, no. 12, pp. 1084–1091, 2021.
- [2] P. A. Stewart, M. Gorman Ng, J. W. Cherrie, A. Jones, R. K. Kwok, A. Blair, L. S. Engel, D. P. Sandler, and M. R. Stenzel, "Estimation of dermal exposure to oil spill response and clean-up workers after the Deepwater Horizon disaster," *Annals of Work Exposures and Health*, vol. 66, no. Supplement_1, pp. i234–i246, 2022.
- [3] K. M. Magalhes, R. S. Carreira, J. S. Rosa Filho, P. P. Rocha, F. M. Santana, and G. T. Yogui, "Polycyclic aromatic hydrocarbons (PAHs) in fishery resources affected by the 2019 oil spill in Brazil: Short-term environmental health and seafood safety," *Marine Pollution Bulletin*, vol. 175, p. 113334, 2022.
- [4] P. A. Sandifer, A. Ferguson, M. L. Finucane, M. Partyka, H. M. Solo-Gabriele, A. H. Walker, K. Wowk, R. Caffey, and D. Yoskowitz, "Human health and socioeconomic effects of the Deepwater Horizon oil spill in the Gulf of Mexico," *Oceanography*, vol. 34, no. 1, pp. 174–191, 2021.
- [5] J. A. Rusiecki, H. Denic-Roberts, D. L. Thomas, J. Collen, J. Barrett, K. Christenbury, and L. S. Engel, "Incidence of chronic respiratory conditions among oil spill responders: Five years of follow-up in the Deepwater Horizon Oil Spill Coast Guard Cohort study," *Environmental Research*, vol. 203, p. 111824, 2022.

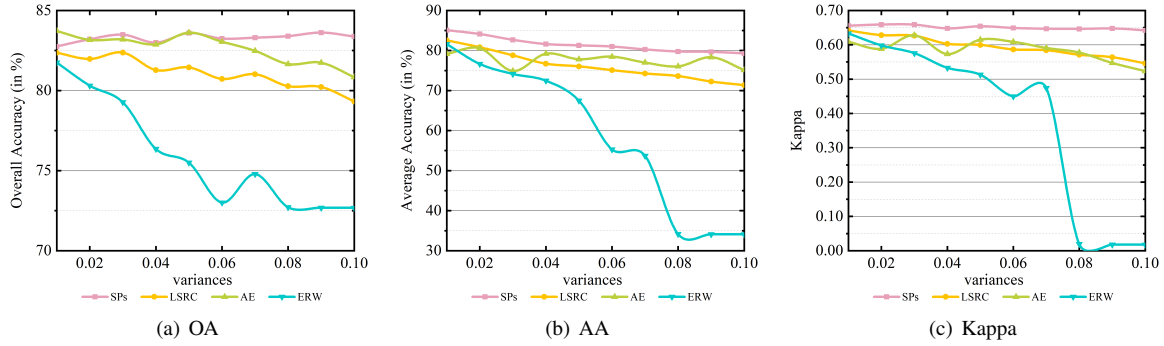


Fig. 12. Classification accuracy of B01 image with different variances of zero-mean Gaussian noise.

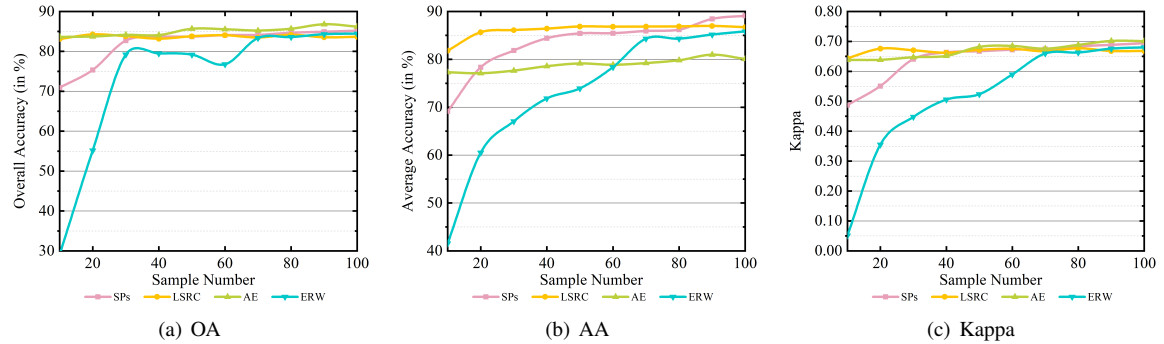


Fig. 13. Classification accuracy of B01 image with different number of training samples.

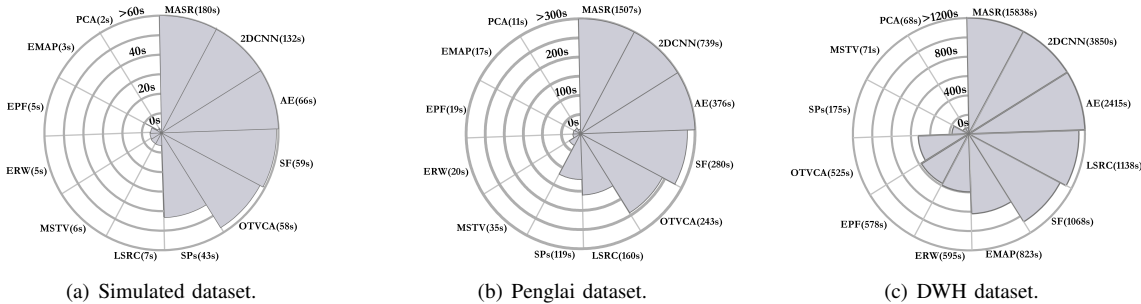


Fig. 14. Computing time of different methods.

- [6] R. A. Magris and T. Giarrizzo, "Mysterious oil spill in the Atlantic Ocean threatens marine biodiversity and local people in Brazil," *Marine pollution bulletin*, vol. 153, p. 110961, 2020.
- [7] R. Jézéquel, J. Guyomarch, J. Receveur, and S. Le Floch, "Effect of long term natural weathering on oil composition: study of the 41-years-old amoco cadiz and 20-years-old erika oil spills," in *International Oil Spill Conference*, vol. 2021, no. 1, 2021, p. 1141297.
- [8] N. Issa and S. Vempatti, "Oil spills in the Arabian Gulf: A case study and environmental review," *Environment and Natural Resources Research*, vol. 8, no. 1, pp. 144–153, 2018.
- [9] E. Cho, M. Park, M. Hur, G. Kang, Y. H. Kim, and S. Kim, "Molecular-level investigation of soils contaminated by oil spilled during the Gulf War," *Journal of Hazardous Materials*, vol. 373, pp. 271–277, 2019.
- [10] F. Qiao, G. Wang, L. Yin, K. Zeng, Y. Zhang, M. Zhang, B. Xiao, S. Jiang, H. Chen, and G. Chen, "Modelling oil trajectories and potentially contaminated areas from the Sanchi oil spill," *Science of the Total Environment*, vol. 685, pp. 856–866, 2019.
- [11] J. Chen, Z. Di, J. Shi, Y. Shu, Z. Wan, L. Song, and W. Zhang, "Marine oil spill pollution causes and governance: A case study of Sanchi tanker collision and explosion," *Journal of Cleaner Production*, vol. 273, p. 122978, 2020.
- [12] I. Castège, E. Milon, and F. Pautrizel, "Response of benthic macrofauna to an oil pollution: Lessons from the Prestige oil spill on the rocky shore of Guéthary (south of the Bay of Biscay, France)," *Deep Sea Research Part II: Topical Studies in Oceanography*, vol. 106, pp. 192–197, 2014.
- [13] A. Sureda, A. Box, S. Tejada, A. Blanco, J. Caixach, and S. Deudero, "Biochemical responses of *Mytilus galloprovincialis* as biomarkers of acute environmental pollution caused by the Don Pedro oil spill (Eivissa Island, Spain)," *Aquatic Toxicology*, vol. 101, no. 3-4, pp. 540–549, 2011.
- [14] M. Lee and J.-Y. Jung, "Pollution risk assessment of oil spill accidents in garorim bay of korea," *Marine Pollution Bulletin*, vol. 100, no. 1, pp. 297–303, 2015.
- [15] A. H. S. Solberg, "Remote sensing of ocean oil-spill pollution," *Proceedings of the IEEE*, vol. 100, no. 10, pp. 2931–2945, 2012.
- [16] S. Mohammadiun, G. Hu, A. A. Gharabagh, J. Li, K. Hewage, and R. Sadiq, "Intelligent computational techniques in marine oil spill management: A critical review," *Journal of Hazardous Materials*, vol. 419, p. 126425, 2021.
- [17] D. Lan, B. Liang, C. Bao, M. Ma, Y. Xu, and C. Yu, "Marine oil spill risk mapping for accidental pollution and its application in a coastal city," *Marine pollution bulletin*, vol. 96, no. 1-2, pp. 220–225, 2015.
- [18] M. Fingas and C. E. Brown, "A review of oil spill remote sensing," *Sensors*, vol. 18, no. 1, p. 91, 2017.
- [19] M. Fingas and C. Brown, "Review of oil spill remote sensing," *Marine Pollution Bulletin*, vol. 83, no. 1, pp. 9–23, 2014.
- [20] J. Plaza, R. Pérez, A. Plaza, P. Martínez, and D. Valencia, "Mapping oil spills on sea water using spectral mixture analysis of hyperspectral image data," in *Chemical and Biological Standoff Detection III*, vol. 5995. Society of Photo-Optical Instrumentation Engineers, 2005, pp. 5995.

- 79–86.
- [21] B. Fiscella, A. Giancaspro, F. Nirchio, P. Pavese, and P. Trivero, “Oil spill detection using marine SAR images,” *International Journal of Remote Sensing*, vol. 21, no. 18, pp. 3561–3566, 2000.
- [22] J. Fan, F. Zhang, D. Zhao, and J. Wang, “Oil spill monitoring based on SAR remote sensing imagery,” *Aquatic Procedia*, vol. 3, pp. 112–118, 2015.
- [23] K. N. Topouzelis, “Oil spill detection by SAR images: dark formation detection, feature extraction and classification algorithms,” *Sensors*, vol. 8, no. 10, pp. 6642–6659, 2008.
- [24] Y. Cheng, X. Li, Q. Xu, O. Garcia-Pineda, O. B. Andersen, and W. G. Pichel, “SAR observation and model tracking of an oil spill event in coastal waters,” *Marine pollution bulletin*, vol. 62, no. 2, pp. 350–363, 2011.
- [25] Q. Zhu, Y. Zhang, Z. Li, X. Yan, Q. Guan, Y. Zhong, L. Zhang, and D. Li, “Oil spill contextual and boundary-supervised detection network based on marine SAR images,” *IEEE Transactions on Geoscience and Remote Sensing*, vol. 60, pp. 1–10, 2022.
- [26] S. Liu, M. Chi, Y. Zou, A. Samat, J. A. Benediktsson, and A. Plaza, “Oil spill detection via multitemporal optical remote sensing images: A change detection perspective,” *IEEE Geoscience and Remote Sensing Letters*, vol. 14, no. 3, pp. 324–328, 2017.
- [27] J. Svejkovsky, W. Lehr, J. Muskat, G. Graettinger, and J. Mullin, “Operational utilization of aerial multispectral remote sensing during oil spill response,” *Photogrammetric Engineering & Remote Sensing*, vol. 78, no. 10, pp. 1089–1102, 2012.
- [28] N. Arslan, “Assessment of oil spills using Sentinel 1 C-band SAR and Landsat 8 multispectral sensors,” *Environmental monitoring and assessment*, vol. 190, no. 11, pp. 1–14, 2018.
- [29] K. Polychronis and K. Vassilia, “Detection of oil spills and underwater natural oil outflow using multispectral satellite imagery,” *International Journal of Remote Sensing Applications*, vol. 3, no. 3, pp. 145–154, 2013.
- [30] F. Salem, M. Kafatos, T. El-Ghazawi, R. Gomez, and R. Yang, “Hyperspectral image analysis for oil spill detection,” in *Summaries of NASA/JPL Airborne Earth Science Workshop, Pasadena, CA*, 2001, pp. 5–9.
- [31] F. S. Uslu, “Kernel parameter variation-based selective ensemble support vector data description for oil spill detection on the ocean via hyperspectral imaging,” *Journal of Applied Remote Sensing*, vol. 11, no. 3, p. 032404, 2017.
- [32] F. Salem, M. Kafatos, T. El-Ghazawi, R. Gomez, and R. Yang, “Hyperspectral image assessment of oil-contaminated wetland,” *International Journal of Remote Sensing*, vol. 26, no. 4, pp. 811–821, 2005.
- [33] Y. Li, Q. Yu, M. Xie, Z. Zhang, Z. Ma, and K. Cao, “Identifying oil spill types based on remotely sensed reflectance spectra and multiple machine learning algorithms,” *IEEE Journal of Selected Topics in Applied Earth Observations and Remote Sensing*, vol. 14, pp. 9071–9078, 2021.
- [34] P. Ghamisi, N. Yokoya, J. Li, W. Liao, S. Liu, J. Plaza, B. Rasti, and A. Plaza, “Advances in hyperspectral image and signal processing: A comprehensive overview of the state of the art,” *IEEE Geoscience and Remote Sensing Magazine*, vol. 5, no. 4, pp. 37–78, 2017.
- [35] M. Imani and H. Ghassemian, “An overview on spectral and spatial information fusion for hyperspectral image classification: Current trends and challenges,” *Information fusion*, vol. 59, pp. 59–83, 2020.
- [36] B. Kumar, O. Dikshit, A. Gupta, and M. K. Singh, “Feature extraction for hyperspectral image classification: A review,” *International Journal of Remote Sensing*, vol. 41, no. 16, pp. 6248–6287, 2020.
- [37] F. Luo, Z. Zou, J. Liu, and Z. Lin, “Dimensionality reduction and classification of hyperspectral image via multistructure unified discriminative embedding,” *IEEE Transactions on Geoscience and Remote Sensing*, vol. 60, pp. 1–16, 2022.
- [38] C. Rodarmel and J. Shan, “Principal component analysis for hyperspectral image classification,” *Surveying and Land Information Science*, vol. 62, no. 2, pp. 115–122, 2002.
- [39] P. Bajorski, “Statistical inference in PCA for hyperspectral images,” *IEEE Journal of Selected Topics in Signal Processing*, vol. 5, no. 3, pp. 438–445, 2011.
- [40] G. Licciardi, P. R. Marpu, J. Chanussot, and J. A. Benediktsson, “Linear versus nonlinear PCA for the classification of hyperspectral data based on the extended morphological profiles,” *IEEE Geoscience and Remote Sensing Letters*, vol. 9, no. 3, pp. 447–451, 2011.
- [41] G. Luo, G. Chen, L. Tian, K. Qin, and S.-E. Qian, “Minimum noise fraction versus principal component analysis as a preprocessing step for hyperspectral imagery denoising,” *Canadian Journal of Remote Sensing*, vol. 42, no. 2, pp. 106–116, 2016.
- [42] A. Villa, J. A. Benediktsson, J. Chanussot, and C. Jutten, “Hyperspectral image classification with independent component discriminant analysis,” *IEEE transactions on Geoscience and remote sensing*, vol. 49, no. 12, pp. 4865–4876, 2011.
- [43] J. Wang and C.-I. Chang, “Independent component analysis-based dimensionality reduction with applications in hyperspectral image analysis,” *IEEE Transactions on Geoscience and Remote Sensing*, vol. 44, no. 6, pp. 1586–1600, 2006.
- [44] J. A. Benediktsson, J. A. Palmason, and J. R. Sveinsson, “Classification of hyperspectral data from urban areas based on extended morphological profiles,” *IEEE Transactions on Geoscience and Remote Sensing*, vol. 43, no. 3, pp. 480–491, 2005.
- [45] B. Rasti, M. O. Ulfarsson, and J. R. Sveinsson, “Hyperspectral feature extraction using total variation component analysis,” *IEEE Transactions on Geoscience and Remote Sensing*, vol. 54, no. 12, pp. 6976–6985, 2016.
- [46] P. Duan, X. Kang, S. Li, and P. Ghamisi, “Noise-robust hyperspectral image classification via multi-scale total variation,” *IEEE Journal of Selected Topics in Applied Earth Observations and Remote Sensing*, vol. 12, no. 6, pp. 1948–1962, June 2019.
- [47] X. Zhang, X. Jiang, J. Jiang, Y. Zhang, X. Liu, and Z. Cai, “Spectral-spatial and superpixelwise pca for unsupervised feature extraction of hyperspectral imagery,” *IEEE Transactions on Geoscience and Remote Sensing*, vol. 60, pp. 1–10, 2022.
- [48] P. Ghamisi, J. Plaza, Y. Chen, J. Li, and A. J. Plaza, “Advanced spectral classifiers for hyperspectral images: A review,” *IEEE Geoscience and Remote Sensing Magazine*, vol. 5, no. 1, pp. 8–32, 2017.
- [49] V. N. Vapnik, “An overview of statistical learning theory,” *IEEE Transactions on Neural Networks*, vol. 10, no. 5, pp. 988–999, 1999.
- [50] L. Gomez-Chova, G. Camps-Valls, J. Munoz-Mari, and J. Calpe, “Semisupervised image classification with laplacian support vector machines,” *IEEE Geoscience and Remote Sensing Letters*, vol. 5, no. 3, pp. 336–340, 2008.
- [51] W.-Y. Loh *et al.*, “Classification and regression tree methods,” *Encyclopedia of Statistics in Quality and Reliability*, vol. 1, pp. 315–323, 2008.
- [52] S. R. Safavian and D. Landgrebe, “A survey of decision tree classifier methodology,” *IEEE Transactions on Systems, Man, and Cybernetics*, vol. 21, no. 3, pp. 660–674, 1991.
- [53] J. Xia, P. Du, X. He, and J. Chanussot, “Hyperspectral remote sensing image classification based on rotation forest,” *IEEE Geoscience and Remote Sensing Letters*, vol. 11, no. 1, pp. 239–243, 2013.
- [54] N. Falco, J. A. Benediktsson, and L. Bruzzone, “Spectral and spatial classification of hyperspectral images based on ica and reduced morphological attribute profiles,” *IEEE Transactions on Geoscience and Remote Sensing*, vol. 53, no. 11, pp. 6223–6240, 2015.
- [55] Y. Li, T. Lu, and S. Li, “Subpixel-pixel-superpixel-based multiview active learning for hyperspectral images classification,” *IEEE Transactions on Geoscience and Remote Sensing*, vol. 58, no. 7, pp. 4976–4988, 2020.
- [56] L. Fang, S. Li, X. Kang, and J. A. Benediktsson, “Spectral-spatial hyperspectral image classification via multiscale adaptive sparse representation,” *IEEE Transactions on Geoscience and Remote Sensing*, vol. 52, no. 12, pp. 7738–7749, 2014.
- [57] M. Zhu, L. Jiao, F. Liu, S. Yang, and J. Wang, “Residual sparsespatial attention network for hyperspectral image classification,” *IEEE Transactions on Geoscience and Remote Sensing*, vol. 59, no. 1, pp. 449–462, Jan 2021.
- [58] P. Ghamisi, J. A. Benediktsson, and M. O. Ulfarsson, “Spectral-spatial classification of hyperspectral images based on hidden markov random fields,” *IEEE Transactions on Geoscience and Remote Sensing*, vol. 52, no. 5, pp. 2565–2574, 2013.
- [59] X. Kang, S. Li, and J. A. Benediktsson, “Spectral-spatial hyperspectral image classification with edge-preserving filtering,” *IEEE Transactions on Geoscience and Remote Sensing*, vol. 52, no. 5, pp. 2666–2677, May 2014.
- [60] X. Kang, S. Li, L. Fang, M. Li, and J. A. Benediktsson, “Extended random walker-based classification of hyperspectral images,” *IEEE Transactions on Geoscience and Remote Sensing*, vol. 53, no. 1, pp. 144–153, Jan 2015.
- [61] L. Wei, Z. Hu, L. Dong, and W. Zhao, “A damage assessment model of oil spill accident combining historical data and satellite remote sensing information: A case study in Penglai 19-3 oil spill accident of China,” *Marine pollution bulletin*, vol. 91, no. 1, pp. 258–271, 2015.
- [62] H. Han, S. Huang, S. Liu, J. Sha, and X. Lv, “An assessment of marine ecosystem damage from the penglai 19-3 oil spill accident,” *Journal of Marine Science and Engineering*, vol. 9, no. 7, p. 732, 2021.

- [63] M. K. McNutt, R. Camilli, T. J. Crone, G. D. Guthrie, P. A. Hsieh, T. B. Ryerson, O. Savas, and F. Shaffer, "Review of flow rate estimates of the deepwater horizon oil spill," *Proceedings of the National Academy of Sciences*, vol. 109, no. 50, pp. 20 260–20 267, 2012.
- [64] E. B. Kujawinski, C. M. Reddy, R. P. Rodgers, J. C. Thrash, D. L. Valentine, and H. K. White, "The first decade of scientific insights from the Deepwater Horizon oil release," *Nature Reviews Earth & Environment*, vol. 1, no. 5, pp. 237–250, 2020.
- [65] C. M. Reddy, J. S. Arey, J. S. Seewald, S. P. Sylva, K. L. Lemkau, R. K. Nelson, C. A. Carmichael, C. P. McIntyre, J. Fenwick, G. T. Ventura *et al.*, "Composition and fate of gas and oil released to the water column during the Deepwater Horizon oil spill," *Proceedings of the National Academy of Sciences*, vol. 109, no. 50, pp. 20 229–20 234, 2012.
- [66] R. O. Green, M. L. Eastwood, C. M. Sarture, T. G. Chrien, M. Aronsson, B. J. Chippendale, J. A. Faust, B. E. Pavri, C. J. Chovit, M. Solis *et al.*, "Imaging spectroscopy and the airborne visible/infrared imaging spectrometer (AVIRIS)," *Remote Sensing of Environment*, vol. 65, no. 3, pp. 227–248, 1998.
- [67] I. Leifer, W. J. Lehr, D. Simecek-Beatty, E. Bradley, R. Clark, P. Dennison, Y. Hu, S. Matheson, C. E. Jones, B. Holt, M. Reif, D. A. Roberts, J. Svejkovsky, G. Swarze, and J. Wozencraft, "State of the art satellite and airborne marine oil spill remote sensing: Application to the bp deepwater horizon oil spill," *Remote Sensing of Environment*, vol. 124, pp. 185–209, 2012.
- [68] A. Lewis, "The development and use of the Bonn Agreement oil appearance code (BAOAC)," in *Proceedings of the Interspill Conference, Cedre, France*, 2009, pp. 12–14.
- [69] R. N. Clark, G. A. Swarze, K. E. Livo, R. F. Kokaly, S. J. Sutley, J. B. Dalton, R. R. McDougal, and C. A. Gent, "Imaging spectroscopy: Earth and planetary remote sensing with the usgs tetracorder and expert systems," *Journal of Geophysical Research: Planets*, vol. 108, no. E12, 2003.
- [70] S. Sun, C. Hu, L. Feng, G. A. Swarze, J. Holmes, G. Graettinger, I. MacDonald, O. Garcia, and I. Leifer, "Oil slick morphology derived from aviris measurements of the deepwater horizon oil spill: Implications for spatial resolution requirements of remote sensors," *Marine Pollution Bulletin*, vol. 103, no. 1, pp. 276–285, 2016.
- [71] X. Kang, X. Xiang, S. Li, and J. A. Benediktsson, "PCA-based edge-preserving features for hyperspectral image classification," *IEEE Transactions on Geoscience and Remote Sensing*, vol. 55, no. 12, pp. 7140–7151, 2017.
- [72] J. Jiang, J. Ma, C. Chen, Z. Wang, Z. Cai, and L. Wang, "SuperPCA: A superpixelwise PCA approach for unsupervised feature extraction of hyperspectral imagery," *IEEE Transactions on Geoscience and Remote Sensing*, vol. 56, no. 8, pp. 4581–4593, 2018.
- [73] M. Dalla Mura, A. Villa, J. A. Benediktsson, J. Chanussot, and L. Bruzzone, "Classification of hyperspectral images by using extended morphological attribute profiles and independent component analysis," *IEEE Geoscience and Remote Sensing Letters*, vol. 8, no. 3, pp. 542–546, 2011.
- [74] L. Xu, Q. Yan, Y. Xia, and J. Jia, "Structure extraction from texture via relative total variation," *ACM Transactions on Graphics (TOG)*, vol. 31, no. 6, pp. 1–10, 2012.
- [75] P. Duan, P. Ghamisi, X. Kang, B. Rasti, S. Li, and R. Gloaguen, "Fusion of dual spatial information for hyperspectral image classification," *IEEE Transactions on Geoscience and Remote Sensing*, vol. 59, no. 9, pp. 7726–7738, 2021.
- [76] J. Mairal, M. Elad, and G. Sapiro, "Sparse representation for color image restoration," *IEEE Transactions on image processing*, vol. 17, no. 1, pp. 53–69, 2007.
- [77] J. Yang, J. Wright, T. S. Huang, and Y. Ma, "Image super-resolution via sparse representation," *IEEE Transactions on Image Processing*, vol. 19, no. 11, pp. 2861–2873, 2010.
- [78] A. M. Bruckstein, D. L. Donoho, and M. Elad, "From sparse solutions of systems of equations to sparse modeling of signals and images," *SIAM Review*, vol. 51, no. 1, pp. 34–81, 2009.
- [79] Y. Xu, Z. Wu, J. Chanussot, and Z. Wei, "Nonlocal patch tensor sparse representation for hyperspectral image super-resolution," *IEEE Transactions on Image Processing*, vol. 28, no. 6, pp. 3034–3047, 2019.
- [80] Y. Chen, N. M. Nasrabadi, and T. D. Tran, "Sparse representation for target detection in hyperspectral imagery," *IEEE Journal of Selected Topics in Signal Processing*, vol. 5, no. 3, pp. 629–640, 2011.
- [81] T. Lu, S. Li, L. Fang, Y. Ma, and J. A. Benediktsson, "Spectral-spatial adaptive sparse representation for hyperspectral image denoising," *IEEE Transactions on Geoscience and Remote Sensing*, vol. 54, no. 1, pp. 373–385, 2015.
- [82] Y. Zhang, Y. Ma, X. Dai, H. Li, X. Mei, and J. Ma, "Locality-constrained sparse representation for hyperspectral image classification," *Information Sciences*, vol. 546, pp. 858–870, 2021.
- [83] S. Li, W. Song, L. Fang, Y. Chen, P. Ghamisi, and J. A. Benediktsson, "Deep learning for hyperspectral image classification: An overview," *IEEE Transactions on Geoscience and Remote Sensing*, vol. 57, no. 9, pp. 6690–6709, 2019.
- [84] V. Sharma, A. Diba, T. Tuytelaars, and L. Van Gool, "Hyperspectral cnn for image classification & band selection, with application to face recognition," *Technical report KUL/ESAT/PSI/1604, KU Leuven, ESAT, Leuven, Belgium*, 2016.
- [85] A. Vaswani, N. Shazeer, N. Parmar, J. Uszkoreit, L. Jones, A. N. Gomez, Ł. Kaiser, and I. Polosukhin, "Attention is all you need," *Advances in Neural Information Processing Systems*, vol. 30, 2017.
- [86] D. So, Q. Le, and C. Liang, "The evolved transformer," in *International Conference on Machine Learning*. PMLR, 2019, pp. 5877–5886.
- [87] J. Xu, J. Yang, X. Xiong, H. Li, J. Huang, K. Ting, Y. Ying, and T. Lin, "Towards interpreting multi-temporal deep learning models in crop mapping," *Remote Sensing of Environment*, vol. 264, p. 112599, 2021.
- [88] D. Hong, Z. Han, J. Yao, L. Gao, B. Zhang, A. Plaza, and J. Chanussot, "Spectralformer: Rethinking hyperspectral image classification with transformers," *IEEE Transactions on Geoscience and Remote Sensing*, vol. 60, pp. 1–15, 2022.
- [89] X. Kang, S. Li, and J. A. Benediktsson, "Feature extraction of hyperspectral images with image fusion and recursive filtering," *IEEE Transactions on Geoscience and Remote Sensing*, vol. 52, no. 6, pp. 3742–3752, 2014.
- [90] M. Abdolmaleki, T. M. Rasmussen, and M. K. Pal, "Exploration of IOCG mineralizations using integration of space-borne remote sensing data with airborne geophysical data," *International Archives of the Photogrammetry, Remote Sensing & Spatial Information Sciences*, vol. 43, pp. 9–16, 2020.
- [91] Y. Chen, Z. Lin, X. Zhao, G. Wang, and Y. Gu, "Deep learning-based classification of hyperspectral data," *IEEE Journal of Selected Topics in Applied Earth Observations and Remote Sensing*, vol. 7, no. 6, pp. 2094–2107, 2014.
- [92] R. Kemker and C. Kanan, "Self-taught feature learning for hyperspectral image classification," *IEEE Transactions on Geoscience and Remote Sensing*, vol. 55, no. 5, pp. 2693–2705, 2017.



Xudong Kang received the B.Sc. degree from Northeast University, Shenyang, China, in 2007, and the Ph.D. degree from Hunan University, Changsha, China, in 2015.

In 2015, he joined the College of Electrical Engineering, Hunan University. His research interests include hyperspectral feature extraction, image classification, image fusion, and anomaly detection.

Dr. Kang received the National Nature Science Award of China (Second Class and Rank as Third) and the Second Prize in the Student Paper Competition at the 2014 International Geoscience and Remote Sensing Symposium (IGARSS). He was selected as the Best Reviewer for the IEEE GEOSCIENCE AND REMOTE SENSING LETTERS and the IEEE TRANSACTIONS ON GEOSCIENCE AND REMOTE SENSING. He was an Associate Editor of the IEEE TRANSACTIONS ON GEOSCIENCE AND REMOTE SENSING from 2018 to 2019. He also serves as an Associate Editor for the IEEE GEOSCIENCE AND REMOTE SENSING LETTERS and the IEEE JOURNAL ON MINIATURIZATION FOR AIR AND SPACE SYSTEMS.



Zihao Wang received the B.S. degree from North China University of Science and Technology, Tangshan, China, in 2020. He is pursuing the M.S. degree with the Laboratory of Vision and Image Processing, Hunan University, Changsha, China.

His research interests include hyperspectral image classification and remote sensing image segmentation.



Puhong Duan received the B.S. degree from Suzhou University, Suzhou, China, in 2014, and the Ph.D. degree from Hunan University, Changsha, China, in 2021.

From October 2019 to December 2019, he was a Visiting Ph.D. Student with the Faculty of Electrical Engineering and Computer Science, Technische Universität Berlin, Berlin, Germany. From January 2020 to October 2020, he was a Visiting Ph.D. Student with the Helmholtz-Zentrum Dresden-Rossendorf, Helmholtz Institute Freiberg for Resource Technology, Freiberg, Germany. He is currently an associate researcher with the College of Electrical and Information Engineering, Hunan University. His research interests include image restoration, multimodal image fusion, and classification.

Dr. Duan was the Finalist for the Best Student Paper Award at the 2020 International Geoscience and Remote Sensing Symposium (IGARSS) and was selected as the Best Reviewer for the IEEE GEOSCIENCE AND REMOTE SENSING LETTERS in 2021. He also serves as an Associate Editor for the FRONTIERS IN REMOTE SENSING.



Xiaohui Wei received the B.S. degree in network engineering from Henan University, Kaifeng, China, in 2014, and the Ph.D. degree in computer science and technology from Hunan University, Changsha, China, in 2019.

He is currently a Post-Doctoral Fellow with the National Engineering Laboratory for Robot Visual Perception and Control Technology, Hunan University.

His research interests include clustering, feature selection, and hyperspectral image processing.